Advances in Water Resources 68 (2014) 24–31

Contents lists available at ScienceDirect

Advances in Water Resources

journal homepage: www.elsevier.com/locate/advwatres

Pore-scale contact angle measurements at reservoir conditions using X-ray microtomography

Matthew Andrew *, Branko Bijeljic, Martin J. Blunt

Qatar Carbonates and Carbon Storage Research Centre, Department of Earth Science and Engineering, Imperial College London, United Kingdom

ARTICLE INFO

Article history:
Received 3 December 2013
Received in revised form 24 February 2014
Accepted 25 February 2014
Available online 12 March 2014

Keywords:
Porescale
Micro-CT
Reservoir condition
Contact angle

ABSTRACT

Contact angle is a principal control of the flow of multiple fluid phases through porous media; however its measurement on other than flat surfaces remains a challenge. A new method is presented for the measurement of the contact angle between immiscible fluids at the pore scale at reservoir conditions (10 MPa and 50 °C) inside a quarry limestone through the use of X-ray microtomography. It is applied to a supercritical CO_2–brine–carbonate system by resampling the micro-CT data onto planes orthogonal to the contact lines, allowing for vectors to be traced along the grain surface and the CO_2–brine interface. A distribution of contact angles ranging from 35° to 55° is observed, indicating that the CO_2–brine–carbonate system is weakly water-wet. This range of contact angles can be understood as the result of contact angle hysteresis and surface heterogeneity on a range of length scales. Surface heterogeneity is examined by comparison of micro-CT results with optical thin sections and SEM images.

1. Introduction

The most important macroscopic parameters for multiphase flow in porous media, such as capillary pressure and relative permeability, are fundamentally controlled by the pore-scale topology, interfacial tension and contact angle [1–3]. This in turn impacts the overall flow behaviour, such as oil and gas recovery [4,5], methane production from hydrate bearing sediments [6–8] and the process of geological CO_2 storage [1,2,9–11].

Wettability is defined as the tendency of one fluid to adhere to a solid surface in the presence of other immiscible fluids [12,13] and is determined, at the pore scale, by the local contact angle (the angle that the interface between two fluid phases makes with the solid, θ, usually measured through the denser phase). The fluid which adheres more readily to the surface is termed the wetting phase. The wetting phase will tend to reside in the smallest areas of the pore-space such as small pores, the corners of larger pores and as connected films residing in the roughness of the solid surface. Conversely, the fluid which adheres less readily, the non-wetting phase, occupies the largest areas of the pore-space, principally in the centres of large pores. The contact angle is related to the interfacial tension of the three interfaces (the solid-non-wetting phase tension, $\gamma_{s\text{-}nw}$, the solid-wetting phase tension, $\gamma_{s\text{-}w}$, and the non-wetting-wetting phase tension, $\gamma_{nw\text{-}w}$) by Young's equation:

$$\gamma_{s-nw} = \gamma_{s-w} + \gamma_{nw-w}\cos\theta \quad (1)$$

As the contact angle controls the arrangement of fluids within the pore-space, its experimental evaluation is vital for a holistic understanding of multiphase flow in geological systems. Traditionally, however, this property could only be accessed directly on pure mineral surfaces, by the use of the dynamic sessile drop method [14,15], the captive bubble method [16] and in micromodel studies [9]. Wettability can be inferred at the core-scale indirectly by the use of the Amott wettability index [17,18]. Even in these simplified systems, results are sparse and inconsistent, especially for supercritical (sc) CO_2–brine–calcite systems. A single study [19] looked at this system using reservoir brines and samples, finding that the CO_2 was non-wetting at low pressures; however they reported that at the reservoir conditions examined here (10 MPa and 50 °C) the system was intermediate wet, with contact angles of around 90°. More data is available with low salinity systems, which seem to be weakly water-wet. Three studies using the same sessile drop method and deionised water report differing angles for CO_2 on calcite. Espinoza and Santamarina [14] examined pressures ranging from 0 to 10 MPa and temperatures of 23.35 °C and found a single angle of 30°. Bikkina [20] considered pressures ranging from 0 to 21 MPa and temperatures of 25 °C and reported little hysteresis between the advancing and receding angle, with both in the range 40–55°. Broseta et al. [21], however, reported much

* Corresponding author. Address: Department of Earth Science and Engineering, South Kensington Campus, Imperial College London, SW7 2AZ, United Kingdom. Tel.: +44 2075941359; fax: +44 2075947444.
E-mail address: m.andrew11@imperial.ac.uk (M. Andrew).

http://dx.doi.org/10.1016/j.advwatres.2014.02.014
0309-1708/

more hysteresis, with advancing (imbibition) angles of 60–75° and receding (drainage) angles of 35–43° at 0.5–14 MPa and 35 °C. Salinity has been observed to be a key control in the $scCO_2$–brine–quartz system, where much more data are available. The system becomes less strongly water-wet as brine salinity is increased, with angles changing from 20° for pure water to 40° when 200 mg/l NaCl is used [14].

Surface roughness has long been recognised as modifying the contact angle in real systems [22,23], so the translation of these disparate values found on ideal, smooth surfaces, to the range of contact angles present in reservoir and aquifer rocks with heterogeneous surface roughness, mineralogical composition and pore topography remains unclear.

Recent advances in microtomography have allowed for the non-invasive imaging of fluid distributions in rocks at conditions of pressure, temperature and salinity representative of oil reservoirs and saline aquifers [24–26]. Experiments examining multiphase flow in a $scCO_2$–brine–rock system must be conducted at these conditions as petrophysical properties (such as surface tension and contact angle) are – as discussed above – strongly pressure and temperature dependent [14]. In this study we propose a new method for characterising the effective contact angle directly in a carbonate–brine–CO_2 system at reservoir/aquifer conditions by the use of microtomography. We choose the carbonate–brine–CO_2 system for two reasons. Firstly, to fill the gap in the literature for such systems; and, secondly, to provide a severe test of the method, since the experiments require the equilibration of $scCO_2$ and the brine, as well as of these fluids with the rock.

2. Method

2.1. Experimental apparatus

The experimental apparatus is shown in Fig. 1; the rock and fluids were imaged using a Versa XRM-500 X-ray Microscope (www.xradia.com). The experiments were conducted on a single carbonate quarry sample, Ketton limestone. Ketton, from the Upper Lincolnshire Limestone Member, is quarried in Ketton, Rutland, UK and was deposited 169–176 million years ago. X-ray diffraction analysis shows this rock type to have an almost pure calcitic mineralogical composition (Table 1).

Table 1
The basic petrophysical properties and mineralogical composition of Ketton limestone. Analysis conducted at Weatherford Laboratories (East Grinstead, UK).

Helium Porosity/ %	Permeability/ m^2	% Calcite	% Quartz	% Feldspar	% Clay
23.37	2.807×10^{-12}	99.1	0.9	0	0

Ketton limestone is an oolitic grainstone, dominated by spherical ooliths up to 600 μm in size. This makes it a good candidate for contact angle studies, as the oolith surface is simpler to trace than those of the more complex pore topography present in, for instance, bioclastic carbonates. It has, however, a signature of heterogeneous flow and transport behaviour, as demonstrated in recent studies [27,28]. The uniform chemical composition also removes the confounding effects of mineralogical heterogeneity, a principal cause of contact angle variation [29]. Samples were drilled into cylindrical cores 4 mm in diameter and 10–20 mm in length. Sample preparation procedures and further details of the apparatus are provided elsewhere [25,26]. The ionic salt used in the brine was Potassium Iodide (KI) with a salinity of 7 wt%. This brine composition was used as KI has a higher X-ray attenuation coefficient than other solute choices (such as NaCl), making it a more effective contrast agent in micro-CT scanning. This allowed for realistic reservoir salinities to be preserved, minimising the relative salinity impact on wettability, as noted in Espinoza and Santamarina [14].

To represent conditions of chemical equilibrium present in the subsurface far away from reservoir or aquifer injection sites, the fluid phases were equilibrated with each other and small particles of the host rock by the use of an entrainment stirrer in a heated reactor (Parr instruments Co., IL, USA). This is necessary, as when CO_2 is injected into a brine-saturated carbonate, the rock will start to dissolve forming a carbonic acid solution, which will affect the contact angle in three ways. Firstly, the dissolution of CO_2 will change the saturation of non-wetting phase in the pore-space. Mass exchange over the CO_2–brine interface will cause the interface to move, possibly affecting the contact angle. Secondly, the carbonic acid will lower the pH of the formation brine. This will start a reaction between the brine and the surface of the oolith. This could change the contact angle, as it could alter both the detail of the surface roughness on the oolith surface and the pore

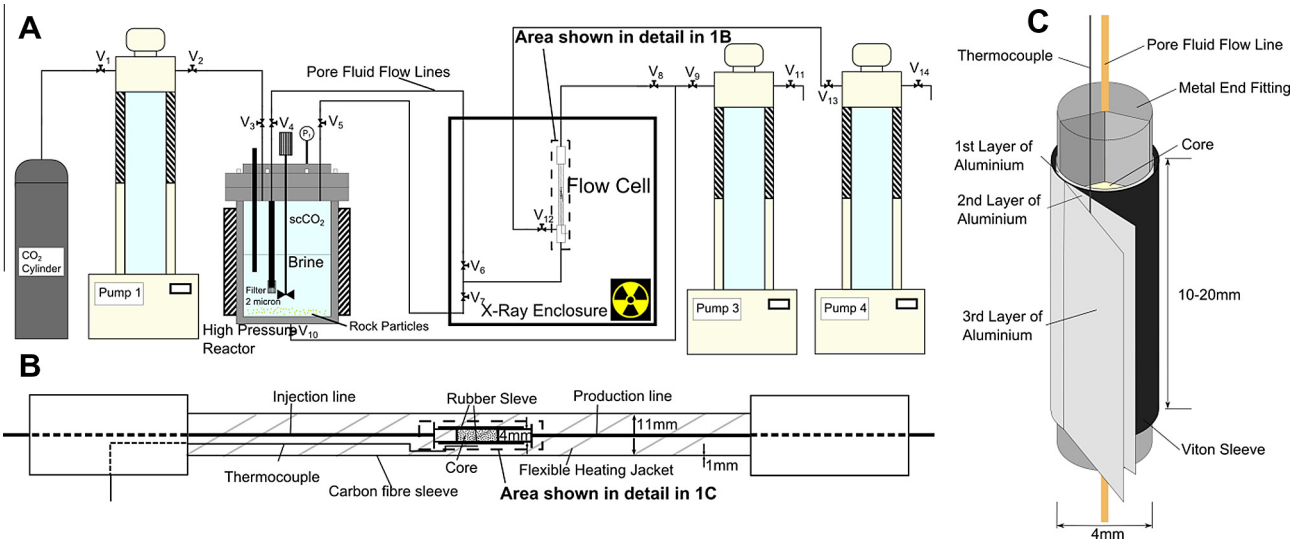

Fig. 1. Experimental apparatus. A: The pumps used to control the flow and the siting of the flow cell within the micro-CT enclosure. B: Detail of the flow cell and heating apparatus and the siting of the core assembly. C: Detail of the core assembly showing a triple wrap of aluminium around the core to prevent diffusive exchange across the Viton sleeve.

morphology, affecting the morphology of the CO_2–brine interface. Finally, the charge balance in the CO_2–brine–carbonate system could shift. This could happen in the brine due to the presence of new active groups created during the formation of carbonic acid and as ions are released into the brine from the solid during the solid-brine reaction. The reaction between the brine and the solid will also change the charge balance of active groups on the solid surface. Any change in charge balance will potentially affect the balance of surface tensions in the CO_2–brine–carbonate system, changing the contact angle. The maintenance of chemical equilibrium in our experiments eliminated these complexities.

2.2. Flow strategy and image acquisition

Contact angle measurements were taken on images where the $scCO_2$ had been trapped as a residual phase, isolated as small droplets in the pore-space. This state was achieved through the following steps.

(1) The pressure and temperature in the reactor was raised to that desired for the pore fluid during the experiment (50 °C and 10 MPa), and was vigorously mixed until no further change in pump volume was seen. This process typically took around 1 h. After this the fluids and solid were mixed for an additional 12 h before the start of the experiment.
(2) A confining pressure of 11 MPa was established within the cell, compressing the Viton sleeve around the core and the metal end-caps, preventing fluid bypass.
(3) The pore space was filled with KI doped brine that had not been equilibrated with $scCO_2$. This was done to dissolve any CO_2 or other gases which may not have been removed by miscible displacement. The temperature and pressure of the core was then raised to those within the reactor, dissolving any residual phases.
(4) More than 1000 pore volumes of equilibrated brine were flushed through the core to miscibly displace the un-equilibrated brine (ensuring 100% initial brine saturation), equilibrate the core grain surfaces with the fluid and create conditions in the core akin to the subsurface conditions in an aquifer at a point slightly ahead of the front of a $scCO_2$ plume. This was judged to be sufficient as no change in the grain surfaces was observed through the entire imaging cycle.
(5) 1 ml (around 20 pore volumes) of $scCO_2$ was passed through the core at very low flow rates (1.67×10^{-9} m^3/s), ensuring a low capillary number of around 10^{-6}. 2D projections were continually taken in order to observe the point when $scCO_2$ displaces brine in the pore space.
(6) 1 ml (around 20 pore volumes) of equilibrated brine was passed though the core at the same low flow rate, causing $scCO_2$ to become trapped as a residual phase in the pore-space.

After step 6, 1600 projections were taken of the sample at regular angular intervals, taking approximately 75 min to acquire. In order to reduce fluid re-arrangement the sample would be left for no more than approximately 20 min prior to image acquisition. The projections were binned from a 2000×2000 grid to a 1000×1000 grid on the camera. These projections were then reconstructed into a 3D volume using proprietary software on the Versa system, creating a reconstructed volume of 1000^3 voxels. The final examined field of view was $2 \times 2 \times 2$ mm. A small voxel size (2.013 μm) was used, so only a central portion of the core was within the field of view. Decreasing the voxel size would have increased image noise due to the effects of more material outside the field of view. It would have also greatly increased scan acquisition time, which would have increased the risk of interface movement during the scan. On the other hand, larger voxels would lead to less accurate identification of the phase interfaces. The ganglia examined in this study contained between 300,000 and 5,000,000 voxels, with a mean ganglion volume of 2,500,000 voxels.

2.3. Image processing

After acquisition the images were filtered using a non-local means edge preserving filter [30,31]. They were then corrected for any beam hardening or softening artefacts created during image reconstruction by modelling these artefacts as radially symmetric Gaussian functions. The centre of this function was allowed to take any point in the x and y dimensions, but was assumed to be uniform in the z direction. As segmentation of images containing a partial saturation of multiple fluids is significantly more difficult than the segmentation of dry images [32], the use of simple grey-scale segmentation was insufficient. Instead a seeded watershed algorithm was used, with the seed generated by the use of a 2D histogram [33]. This segmented image was then analysed in 3D to identify each unique disconnected ganglion, which was then labelled.

A subvolume was then extracted around each unique ganglion and resegmented using the same 2D histogram-based watershed method detailed above, as the beam hardening and softening correction may not remove all lateral variations in grey-scale value across the image. Local segmentation was therefore likely to be more accurate than the primary global segmentation.

The edges of each phase were found on this new segmented image using a 3D Sobel filter [13]. The intersection of the edges of all three phases ($scCO_2$, brine and solid) was labelled as the contact line which could be traced in 3D. Finally a bilinear filter was applied to the resampled slice to eliminate possible angular quantisation due to the voxelized nature of the image. The contact angle was then measured by resampling the data onto a plane with a normal parallel to the contact line at a specific point (Fig. 2). The measurement was taken according to the best interpretation of the tangential direction of the relevant surfaces at the contact line and no effort to "smooth" the surfaces was made. This can be seen in Fig. 3F, where the tangential direction on the grain surface at the contact point is seen to be at a significant angle to the larger scale attitude of the grain surface. The resulting variation in contact angle was reported as part of the distribution shown in Fig. 4.

Contact angles were measured manually on the unsegmented data by tracing two vectors tangential to the $scCO_2$–brine interface and the rock surface. The angle between these lines was then measured through the non-wetting phase with a 3D angle measurement tool (Fig. 3). Measurements were performed at 300 points randomly selected along the $scCO_2$–brine–rock contact lines of different ganglia. The contact angle was not measured on the segmented data, as the angle measured was highly sensitive to the detail of segmentation close to the contact line, where we would expect the segmentation to be least accurate. In contrast, tracing the interface between the $scCO_2$ and the brine visually was relatively simple, making angle measurement more accurate and robust.

All image processing was conducted within the Avizo Fire 8.0 (Visual Sciences Group, www.vsg3d.com) and imageJ programs.

3. Results and discussion

$scCO_2$ was universally seen to be the non-wetting phase in this system with a mean contact angle (as measured through the brine) of 45° and an approximately symmetric range around this mean of

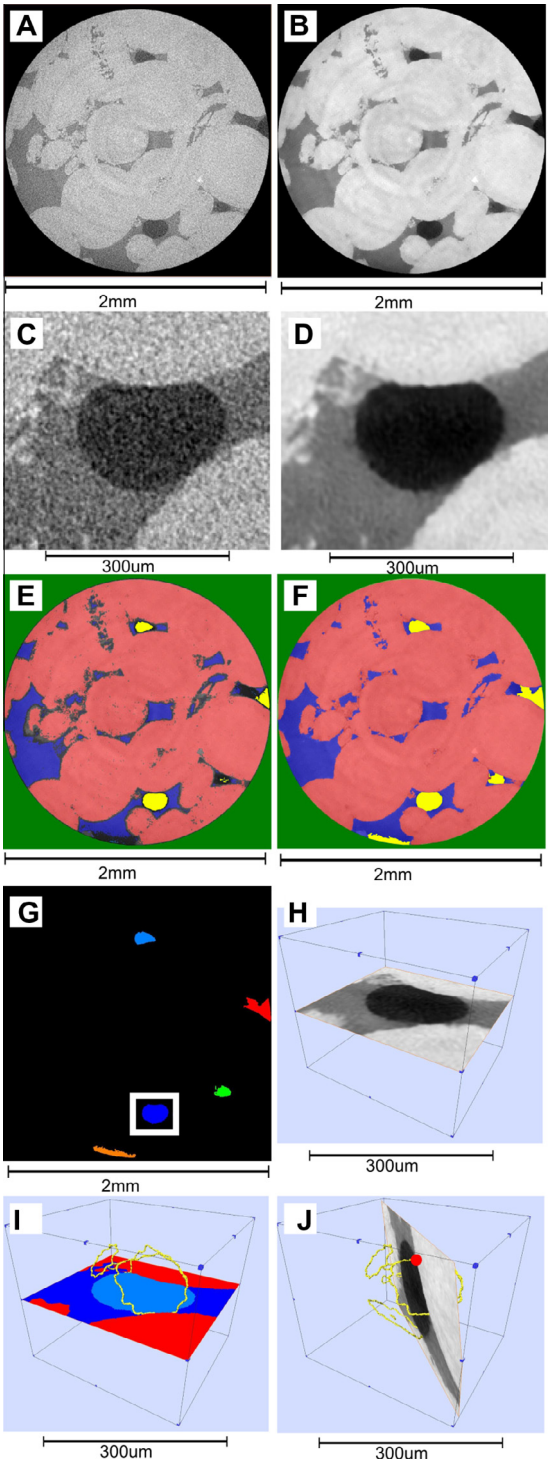

Fig. 2. The image processing workflow. The darkest phase is $scCO_2$, the intermediate phase is brine and the lightest phase is solid. A: The raw reconstructed image. B: The filtered image, filtered using a non-local means edge preserving filter and corrected for beam softening. C: A higher resolution subsection of the raw reconstructed image. D: This subsection filtered using a non-local means edge preserving filter. E: The watershed seed image, generated by labelling voxels using a 2D histogram. F: The expanded label image found by growing the seed shown in D with a watershed algorithm. G: A map of the ganglia present within the segmented image. H: A subvolume of the unsegmented data. The subvolume shown in H–J is shown as a white rectangle in G. H–J. The data were resegmented using a 2D histogram watershed segmentation. The contact line is shown as a yellow line rendered in 3D. J: The data were resampled onto a plane with a normal parallel to the contact line at a point indicated by the red dot. (For interpretation of the references to colour in this figure legend, the reader is referred to the web version of this article.)

10°: the standard deviation in the measured value is 6°. The distribution of contact angles as measured on all the ganglia in the image can be seen in Fig. 4.

This distribution can be explained as the result of multiple contributing factors. Firstly, we would expect to see hysteresis between the advancing and receding contact angle. This is caused by pinning of the contact line to a single spot on the solid surface. During wetting phase advance, small increases in the brine pressure, perturbing the fluid–fluid interface, will not move the contact line. The contact angle will increase until some threshold maximal contact angle (the advancing contact angle) is exceeded, where the contact line will start to move. Conversely, during the recession of the wetting phase the contact angle will approach a minimum (the receding angle) before contact line movement (Fig. 5). The images are taken at the end of imbibition, during which the wetting phase swells displacing $scCO_2$. During this process advancing contact angles will be present; however some rearrangement of the fluid interfaces after injection has finished is possible: we discuss this in more detail later.

The main sources of this hysteresis are roughness in the solid surface, adsorption effects and surface impurities [29,34–36]. Even when contact angle is measured on crystal surfaces, moderate hysteresis is seen, with receding (drainage) contact angles ranging from 35° to 43° and advancing (imbibition) angles ranging from 60° to 75° for the $scCO_2$–calcite–water system, as mentioned previously [21]. As the grain surface in real rocks is heterogeneous we would expect this heterogeneity to cause a distribution in observed contact angles. Grain surface heterogeneity can be seen at larger scales, such that they are visible on the micro-CT scan, as small protrusions in the solid surface that can inhibit the movement of the contact line. This will effectively pin the contact line at a single point, causing the contact angle to change in response to changes in fluid pressure. The resulting arrangement of fluids will then be dependent on these small details of the pore topography (Fig. 6).

At smaller scales, not visible on the micro-CT scan, changes in the surface roughness can be seen qualitatively in optical thin section (Fig. 7) and scanning electron microscope (SEM) images (Fig. 8). Optical thin sections show the interior structure of grains much more clearly than micro-CT images, making surface differences more obvious, whereas SEM images can be taken at a much higher resolution than either micro-CT or optical thin section images.

Another contribution to the contact angle distribution, shown in Fig. 9, is the relaxation of the advancing contact angle to the equilibrium angle. If the advancing or receding interfaces are allowed to come to rest, then the contact angle should approach a common equilibrium value over time [37,38]. This process was observed in our study as an apparent intermediate phase appearing on the interface near the contact point (Fig. 9), caused by the interface moving during the scan. One interpretation of this interface movement is the relaxation of an advancing contact angle (after waterflooding) to an equilibrium position once injection has stopped and the fluids come to rest. This caused the reconstructed voxels to have a greyscale intermediate between the greyscale of the two fluid phases. The rate at which this occurs may be different at different points along the contact line, leading to a distribution of the apparent contact angle. It is possible that small changes in interface position, causing the presence of this apparent intermediate phase could also be caused by changes in ganglion volume due to small changes in temperature and solubility during the period of the scan.

Finally, measurement uncertainty cannot be eliminated. Two sources of measurement uncertainty can be identified: a misidentification of the resampling plane; and, once the resampling plane has been identified, the incorrect identification of the vectors

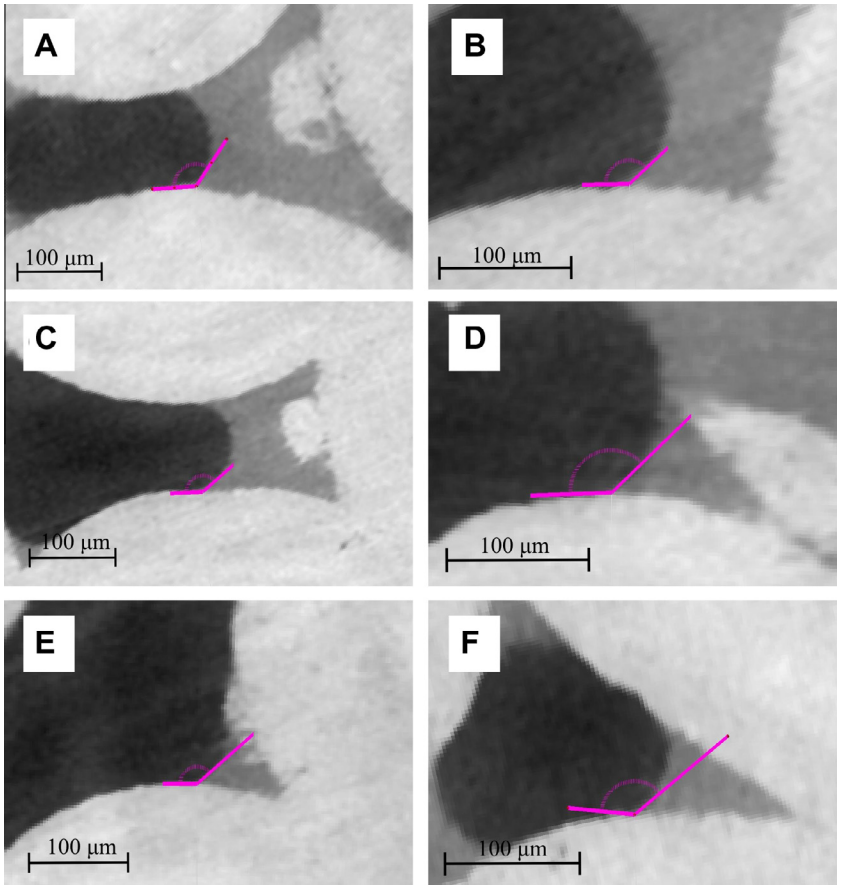

Fig. 3. Six contact angles measured on the resampled data. The angles were measured through the dark non-wetting phase (the $scCO_2$), shown by the pink arc; however the quoted angles are the complement – measured through the wetting (denser–grey) phase. The angles measured in each of these cases are A: 53°, B: 42°, C: 39°, D: 41°, E: 43°, F: 46°. (For interpretation of the references to colour in this figure legend, the reader is referred to the web version of this article.)

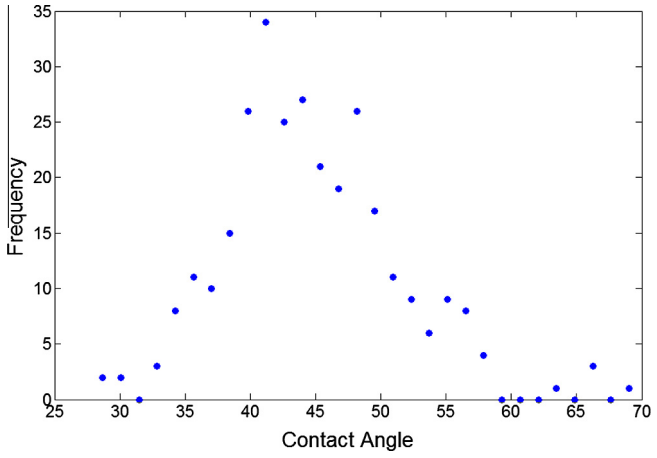

Fig. 4. A histogram of the distribution of contact angles.

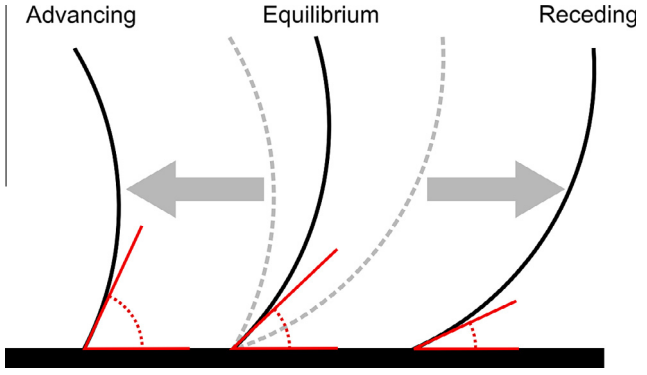

Fig. 5. Hysteresis in the contact angle is expected. During wetting phase advance (imbibition) the contact angle will be larger than at equilibrium. During wetting phase recession (drainage) the contact angle will be smaller than at equilibrium. The grey arrows show the direction of interface movement. The dotted grey lines show the three different interface positions superposed on each other.

tangential to the CO_2–brine interface and the rock surface. Although there may be some error in the identification of the triple point at any particular point along the contact line, a particular advantage of this approach is that the direction of the contact line will be well determined, as the positional error of the triple point is small compared to the length of the contact line. Any error in the determination of the triple point should be systematic, as the segmentation is always performed in the same way, so the direction of the contact line should be preserved. We estimate angular errors to the attitude of the resampling plane to be small, at most 5–10°. To quantify the impact this would have on measured contact angles, the resampling plane was rotated around two axes, perpendicular and parallel to the grain surface. Contact angles were measured at regular angular intervals, and the results can be seen in Fig. 10. Large changes in the measured contact angle do not occur until angular errors of around 20–30° in the attitude of the resampling plane, so we would expect this error to be small.

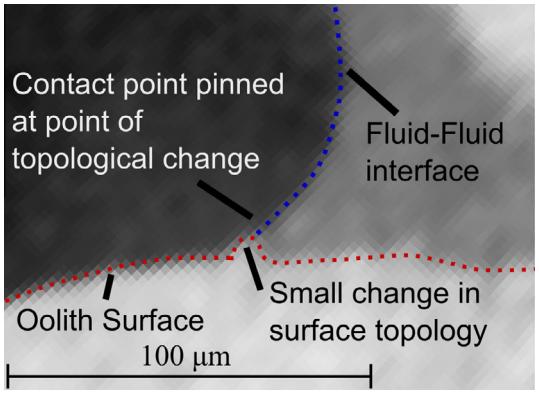

Fig. 6. Small changes in the oolith surface can pin the contact line, changing the apparent contact angle as the fluid pressure changes.

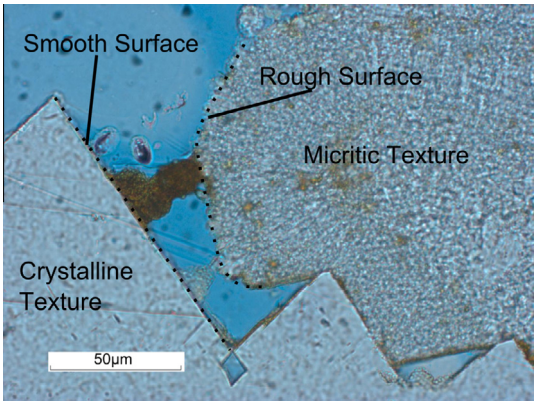

Fig. 7. Surface roughness variations can be seen in optical thin section. The micritic texture is associated with a rough surface where crystalline texture is associated with a much smoother surface.

Another source of error is the incorrect identification of the CO_2–brine interface and the grain surface, an ambiguity which can be seen in Fig. 3F. The primary control on this is the ratio of the spatial length scale for variation in the surface to the voxel size. The spatial length scale for variation of a particular interface can be quantified by fitting a surface to it and measuring its curvature. This curvature can be determined by creating best fit quadratic surfaces, with well-defined curvatures, at each point along the generated surface, as detailed in [39]. A distribution of these curvatures for the CO_2–brine interface and the grain surface of a typical residual ganglion is shown in Fig. 11. The curves represent Gaussian distributions fitted to each curvature distribution. The average radius of curvature for the CO_2–brine interface is 53 times

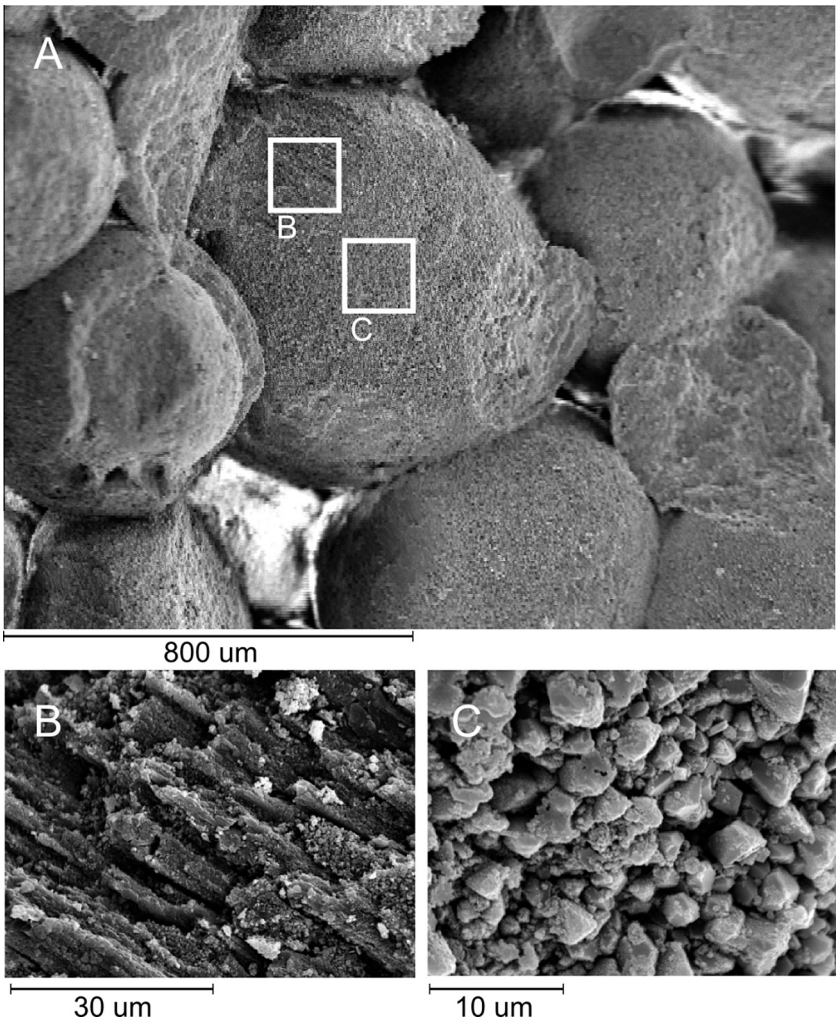

Fig. 8. A: Spherical ooliths can be seen on low resolution SEM images. Zooming in on area B shows a relatively smooth surface texture, where zooming in on area C shows a much rougher surface texture.

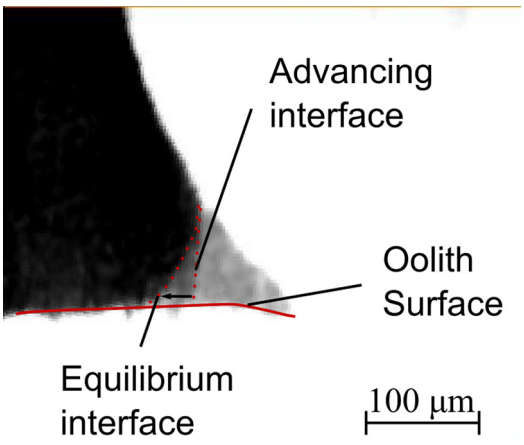

Fig. 9. One factor contributing to the contact angle distribution is regression of the contact angle towards the equilibrium contact angle over time. The shaded region represents movement of the brine–scCO$_2$ interface during the scan. The arrow shows the direction of interface movement during the scan.

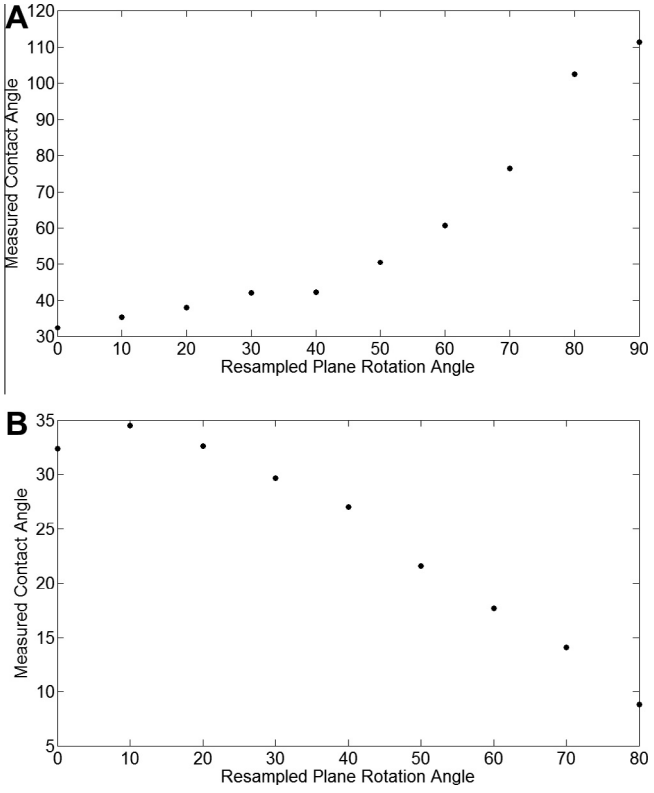

Fig. 10. The sensitivity of contact angle to errors in the attitude of the resampling plane. A: The variation in contact angle as the resampling plane is rotated about a plane parallel to the grain surface. B: The variation in measured contact angle as the resampling plane is rotated about a plane perpendicular to the grain surface.

the size of each individual voxel, and the average grain radius of curvature for the grain surface is 238 times the voxel size. As the typical length scale for spatial variation in the interfaces is orders of magnitude larger than the voxel size, errors in identification of the tangential vectors are correspondingly small. Furthermore, one of the principal advantages of this technique is that it allows for many measurements to be taken very rapidly, allowing for statistical distributions to be seen (Fig. 4). The measurement error associated with taking each individual measurement manually should be random, therefore its relative impact should decrease in-

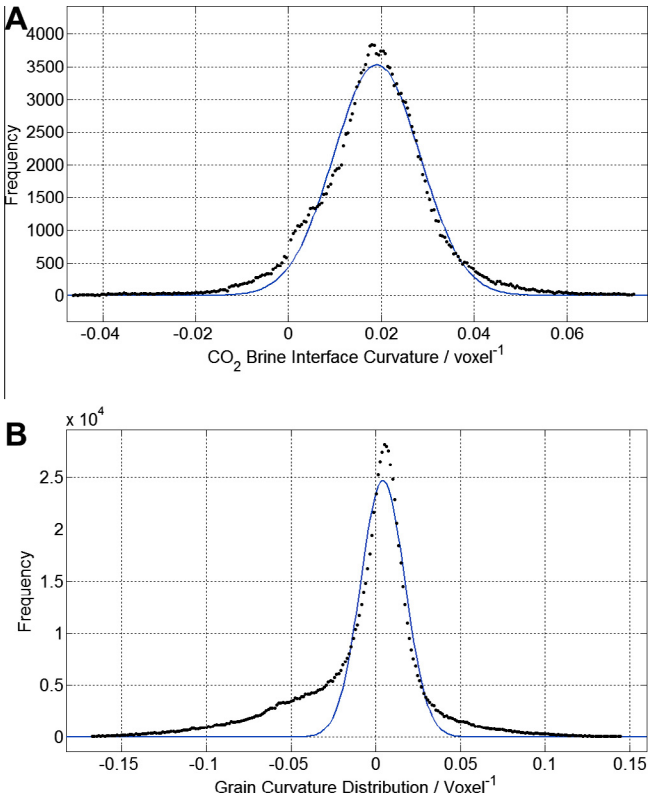

Fig. 11. The spatial length scale for surface variation is estimated by calculating the surface curvature of a surface generated from grains and CO_2–brine interface around a representative ganglion. A shows the curvature distribution of the CO_2–brine interface. The typical radius of curvature is 53 times the voxel size. B shows the curvature distribution of the grain surface. The typical radius of curvature is 238 times the voxel size.

versely proportional to $\sqrt{n}$, where n is the number of measurements.

All of these processes contribute to the distribution of contact angle seen in Fig. 4; the overall effect is to see a range of contact angles spanning approximately 30°. Larger impacts on the contact angle, such as the precipitation of asphaltenes on grain surfaces in oil reservoirs, or the use of surfactants for enhanced oil recovery, should be measurable and could be the target of further study. Although this method may not be applicable for rock types with pores that cannot be resolved by micro-CT scanning, for example shales, there is a wide range of systems for which it could be of great utility. The method for assessing the spatial length scale for variation of a surface outlined above could be extrapolated in future work to examine rocks with extremely complex pore topography, generating maps of surface roughness in order to target contact angle measurements to areas of interest, to describe the pore by pore impact of surface roughness on resulting contact angle distributions. This method could also be combined with recent developments in the generation of mineral mapping [40,41] to examine the impact of mineral heterogeneity on the distribution of wettability.

This work contradicts some measurements of contact angle in the scCO$_2$–brine–carbonate system, which was found to be intermediate-wet, with contact angles around 90° [19], but are consistent with trapping results on a scCO$_2$–brine–limestone system, where significant proportions of CO_2 are trapped as a residual phase [25,26,42] indicating that the system is water-wet. This consistency supports this new method as a choice for wettability determination in specific systems, especially considering the difficulty in application of results from traditional methods such as the

sessile drop. Furthermore, this measured distribution of contact angles could be input into pore-scale models to predict multiphase flow properties, such as capillary pressure and relative permeability [43].

4. Conclusions

We present a new method for measuring the contact angle of multiple immiscible fluids, applied to a $scCO_2$–brine–carbonate system, at pressures and temperatures representative of flow in subsurface hydrocarbon reservoirs and aquifers (10 MPa and 50 °C) using micro-CT imaging. The micro-CT data are resampled onto a plane perpendicular to the contact line and then measured manually by tracing vectors tangential to the solid surface and the $scCO_2$–brine interface. This was done at 300 locations on an image of $scCO_2$ trapped as a residual phase in the pore-space of the $scCO_2$. This system was universally weakly water-wet with an average contact angle of 45 ± 6°. The distribution of contact angles can be understood as the result of the multiple contributing factors of contact angle hysteresis and surface heterogeneity on a range of length scales. This measurement can be used as an input for pore-scale models. The technique has potential applicability to a wide range of problems in multiphase flow in porous media, from the development of mixed-wet reservoirs to the use of surfactants in contaminant transport.

Acknowledgements

We gratefully acknowledge funding from the Qatar Carbonates and Carbon Storage Research Centre (QCCSRC), provided jointly by Qatar Petroleum, Shell, and Qatar Science & Technology Park. We also acknowledge funding from the Imperial College Consortium on Pore-Scale Modelling.

References

[1] Chalbaud C, Robin M, Lombard JM, Bertin J, Egermann P. Brine/CO_2 interfacial properties and effects on CO_2 storage in deep saline aquifers. Oil Gas Sci Technol – Rev IFP 2010;65:541–55. http://dx.doi.org/10.2516/ogst/2009061.
[2] Plug WJ, Bruining J. Capillary pressure for the sand–CO_2–water system under various pressure conditions. Application to CO_2 sequestration. Adv Water Resour 2007;30:2339–53. http://dx.doi.org/10.1016/j.advwatres.2007.05.010.
[3] Gaus I. Role and impact of CO_2–rock interactions during CO_2 storage in sedimentary rocks. Int J Greenhouse Gas Control 2010;4:73–89. http://dx.doi.org/10.1016/j.ijggc.2009.09.015.
[4] Pope GA, Baviere M. Reduction of capillary forces by surfactants. In: Baviere M, editor. Basic concepts in enhanced oil recovery processes. London: Elsevier Applied Science; 1991.
[5] Rosen MJ, Wang H, Shen P, Zhu Y. Ultralow interfacial tension for enhanced oil recovery at very low surfactant concentrations. Langmuir 2005;21:3749–56. http://dx.doi.org/10.1021/la0400959.
[6] Seo Y, Lee H, Uchida T. Methane and carbon dioxide hydrate phase behavior in small porous silica gels: three-phase equilibrium determination and thermodynamic modeling. Langmuir 2002;18:9164–70. http://dx.doi.org/10.1021/la0257844.
[7] Sun CY, Chen GJ, Yang LY. Interfacial tension of methane + water with surfactant near the hydrate formation conditions. J Chem Eng Data 2004;49:1024–5. http://dx.doi.org/10.1021/je049948p.
[8] Watanabe K, Imai S, Mori YH. Surfactant effects on hydrate formation in an unstirred gas/liquid system: an experimental study using HFC-32 and sodium dodecyl sulfate. Chem Eng Sci 2005;60:4846–57. http://dx.doi.org/10.1016/j.ces.2005.03.043.
[9] Chalbaud C, Robin M, Lombard JM, Martin F, Egermann P, Bertin J. Interfacial tension measurements and wettability evaluation for geological CO_2 storage. Adv Water Resour 2009;32:98–109. http://dx.doi.org/10.1016/j.advwatres.2008.10.012.
[10] Chiquet P, Broseta D, Thibeau S. Wettability alteration of caprock minerals by carbon dioxide. Geofluids 2007;7:112–22. http://dx.doi.org/10.1111/j.1468-8123.2007.00168.x.
[11] Hildenbrand A, Schlomer S, Krooss BM, Littke R. Gas breakthrough experiments on pelitic rocks: comparitive study with N_2, CO_2 and CH_4. Geofluids 2004;4:61–80.
[12] Forrest C. The reservoir engineering aspects of waterflooding, SPE monograph series. Texas: Society of Petroleum Engineers; 1993. vol. 3.
[13] Engel K, Hadwiger M, Kniss J, Rezk-Salama C, Weiskopf D. Real-time volume graphics. Natick, USA: A K Peters; 2006.
[14] Espinoza DN, Santamarina JC. Water–CO_2–mineral systems: interfacial tension, contact angle, and diffusion-Implications to CO_2 geological storage. Water Resour Res 2010;46. http://dx.doi.org/10.1029/2009WR008634.
[15] Dickson JL, Gupta G, Horozov TS, Binks BP, Johnston KP. Wetting phenomena at the CO_2/water/glass interface. Langmuir 2006;22:2161.
[16] Chiquet P, Daridon JL, Broseta D, Thibeau S. CO_2/water interfacial tensions under pressure and temperature conditions of CO_2 geological storage. Energy Convers Manage 2007;48:736–44.
[17] Amott E. Observations Relating to the Wettability of Porous Rock. SPE-1167-G. Petroleum Transactions. AIME 1959;216:156–62.
[18] Abdallah WJ, Buckley J, Carnegie A, Edwards J, Herold B, Fordham EJ, et al. Fundamentals of wettability. Oilfield Rev. 2007;19.
[19] Yang D, Gu Y, Tontiwachwuthikul P. Wettability determination of the reservoir brine–reservoir rock system with dissolution of CO_2 at high pressures and elevated temperatures. Energy Fuels 2008;22:504–9. http://dx.doi.org/10.1021/ef700383x.
[20] Bikkina PK. Contact angle measurements of CO_2–water–quartz/calcite systems in the perspective of carbon sequestration. Int J Greenhouse Gas Control 2011;5:1259–71. http://dx.doi.org/10.1016/j.ijggc.2011.07.001.
[21] Broseta D, Tonnet N, Shah V. Are rocks still water-wet in the presence of dense CO_2 or H_2S? Geofluids 2012;12:280–94. http://dx.doi.org/10.1111/j.1468-8123.2012.00369.x.
[22] Wenzel RN. Resistance of solid surfaces to wetting by water. Ind Eng Chem 1936;28:988–94.
[23] Cassie ABD, Baxter S. Wettability of porous surfaces. Trans Faraday Soc 1944;40:546–51.
[24] Iglauer S, Paluszny A, Pentland CH, Blunt MJ. Residual CO_2 imaged with X-ray micro-tomography. Geophys Res Lett 2011;38. http://dx.doi.org/10.1029/2011GL049680.
[25] Andrew MG, Bijeljic B, Blunt MJ. Pore-scale imaging of geological carbon dioxide storage under in situ conditions. Geophys Res Lett 2013;40:3915–8.
[26] Andrew MG, Bijeljic B, Blunt MJ. Pore-scale imaging of trapped supercritical carbon dioxide in sandstones and carbonates. Int J Greenhouse Gas Control 2014;22:1–14.
[27] Bijeljic B, Mostaghimi P, Blunt MJ. Insights into non-Fickian solute transport in carbonates. Water Resour Res 2013;49:2714–28. http://dx.doi.org/10.1002/wrcr.20238.
[28] Bijeljic B, Raeini A, Mostaghimi P, Blunt MJ. Predictions of non-Fickian solute transport in different classes of porous media using direct simulation on pore-scale images. Phys Rev E 2013;87:013011-1–9. http://dx.doi.org/10.1103/PhysRevE.87.013011.
[29] de Gennes PG. Wetting: statics and dynamics. Rev Mod Phys 1985;57:827–63. http://dx.doi.org/10.1103/RevModPhys.57.827.
[30] Buades A, Coll B, Morel J-M. A non-local algorithm for image denoising. Comput Vision Pattern Recognit 2005.
[31] Buades A, Coll B, Morel J-M. Nonlocal image and movie denoising. Int J Comput Vision 2008;76:123–39. http://dx.doi.org/10.1007/s11263-007-0052-1.
[32] Sheppard AP, Sok RM, Averdunk H. Techniques for image enhancement and segmentation of tomographic images of porous materials. Phys A 2004;339:145–51. http://dx.doi.org/10.1016/j.physa.2004.03.057.
[33] Jones AC, Arns CH, Sheppard AP, Hutmacher DW, Milthorpe BK, Knackstedt MA. Assessment of bone ingrowth into porous biomaterials using MICRO-CT. Imaging Tech Biomater Charact 2007;28:2491–504. http://dx.doi.org/10.1016/j.biomaterials.2007.01.046.
[34] Hillel D. Fundamentals of soil physics. San Diego, California: Academic; 1980.
[35] Miller CA, Noegi P. Interfacial phenomena. New York: Marcel Dekker; 1985.
[36] Schiegg HO. Evaluation and treatment of cases of oil damage with regard to groundwater protection. Zurich: Swiss Federal Office of the Environment; 1986.
[37] Hassanizadeh SM, Gray WG. Thermodynamic basis of capillary pressure in porous media. Water Resour Res 1993;29:3389–405.
[38] Bartell FE, Merrill EJ. Determination of adhesion tension of liquids against solids: a microscopic method for the measurement of contact angle. J Phys Chem 1932;36:1178–90.
[39] Armstrong RT, Porter ML, Wildenschild D. Linking pore-scale interfacial curvature to column-scale capillary pressure. Adv Water Resour 2012;46:55–62.
[40] Cnudde V, Boone MN. High-resolution X-ray computed tomography in geosciences: a review of the current technology and applications. Earth Sci Rev 2013;123:1–17. http://dx.doi.org/10.1016/j.earscirev.2013.04.003.
[41] Golab A, Knackstedt MA, Averdunk H, Senden T, Butcher A, Jaime P. 3D porosity and mineralogy characterization in tight gas sandstones. Leading Edge 2010;29:1476–83. http://dx.doi.org/10.1190/1.3525363.
[42] El-Maghraby RM, Blunt MJ. Residual CO_2 trapping in Indiana limestone. Environ Sci Technol 2013;47:227–33. http://dx.doi.org/10.1021/es304166u.
[43] Blunt MJ, Bijeljic B, Dong H, Gharbi O, Iglauer S, Mostaghimi P, et al. Pore-scale imaging and modelling. Adv Water Resour 2013;51:197–216. http://dx.doi.org/10.1016/j.advwatres.2012.03.003.